

# A spectroscopically confirmed, strongly lensed, metal-poor Type II supernova at $z = 5.13$

David A. Coulter<sup>1,2\*†</sup>, Conor Larison<sup>2\*†</sup>, Justin D. R. Pierel<sup>2</sup>, Seiji Fujimoto<sup>3,4</sup>,  
Vasily Kokorev<sup>5,6</sup>, Joseph F. V. Allingham<sup>7</sup>, Takashi J. Moriya<sup>8,9,10</sup>, Matthew Siebert<sup>2</sup>,  
Yoshihisa Asada<sup>3</sup>, Rachel Bezanson<sup>11</sup>, Maruša Bradač<sup>12,13</sup>, Gabriel Brammer<sup>14</sup>,  
John Chisholm<sup>5,6</sup>, Dan Coe<sup>2</sup>, Pratika Dayal<sup>3,15,16</sup>, Michael Engesser<sup>2</sup>,  
Steven L. Finkelstein<sup>5,6</sup>, Ori D. Fox<sup>2</sup>, Lukas J. Furtak<sup>5,6</sup>, Anton M. Koekemoer<sup>2</sup>,  
Thomas Moore<sup>2</sup>, Minami Nakane<sup>17,18</sup>, Masami Ouchi<sup>8,17,9,19</sup>, Richard Pan<sup>20</sup>,  
Robert Quimby<sup>21,19</sup>, Armin Rest<sup>2,1</sup>, Johan Richard<sup>22</sup>, Luke Robbins<sup>20</sup>,  
Louis-Gregory Strolger<sup>2</sup>, Fengwu Sun<sup>23</sup>, Tommaso Treu<sup>24</sup>, Hiroto Yanagisawa<sup>17,18</sup>,  
Abdurro'uf<sup>25</sup>, Aadya Agrawal<sup>26</sup>, Ricardo Amorín<sup>27</sup>, Joseph P. Anderson<sup>28</sup>,  
Rodrigo Angulo<sup>1</sup>, Hakim Atek<sup>29</sup>, Franz E. Bauer<sup>30</sup>, Larry D. Bradley<sup>2</sup>, Volker Bromm<sup>5,6</sup>,  
Mateusz Bronikowski<sup>31</sup>, Christopher J. Conselice<sup>32</sup>, Christa DeCoursey<sup>33</sup>,  
James M. DerKacy<sup>2</sup>, Guillaume Desprez<sup>34</sup>, Suhail Dhawan<sup>35</sup>, Jose M. Diego<sup>36</sup>,  
Eiichi Egami<sup>33</sup>, Andreas Faisst<sup>37</sup>, Brenda Frye<sup>33</sup>, Sebastian Gomez<sup>5</sup>,  
Mauro González-Otero<sup>27</sup>, Massimo Griggio<sup>2</sup>, Yuichi Harikane<sup>17</sup>, Kohei Inayoshi<sup>38</sup>,  
Saurabh W. Jha<sup>39</sup>, Yolanda Jiménez-Teja<sup>27,40</sup>, Jeyhan S. Kartaltepe<sup>41</sup>, Patrick L. Kelly<sup>42</sup>,  
Lindsey A. Kwok<sup>43</sup>, Zachary G. Lane<sup>44</sup>, Xiaolong Li<sup>1</sup>, Ivo Lobbe<sup>45</sup>, Paulo A. A. Lopes<sup>46</sup>,  
Ray A. Lucas<sup>2</sup>, Georgios E. Magdis<sup>14,47</sup>, Nicholas S. Martis<sup>12</sup>, Jorryt Matthee<sup>48</sup>,  
Ashish K. Meena<sup>49</sup>, Rohan P. Naidu<sup>50</sup>, Gaël Noiro<sup>2</sup>, Masamune Oguri<sup>51,52</sup>,  
Estefania Padilla Gonzalez<sup>1</sup>, Massimo Pascale<sup>24</sup>, Tanja Petrushevska<sup>31</sup>, Massimo Ricotti<sup>53</sup>,

Daniel Schaefer<sup>54</sup>, Stefan Schuldt<sup>55,56,57</sup>, Melissa Shahbandeh<sup>2</sup>, William Sheu<sup>24</sup>,  
Koji Shukawa<sup>1</sup>, Akiyoshi Tsujita<sup>58</sup>, Eros Vanzella<sup>59</sup>, Qinan Wang<sup>50</sup>, John Weaver<sup>50</sup>,  
Robert Williams<sup>2,60</sup>, Rogier Windhorst<sup>61</sup>, Yi Xu<sup>14</sup>, Yossef Zenati<sup>1,62,63</sup>, Adi Zitrin<sup>7</sup>

<sup>1</sup>William H. Miller III Department of Physics and Astronomy, Johns Hopkins University, 3400 North Charles Street, Baltimore, MD 21218, USA.

<sup>2</sup>Space Telescope Science Institute, 3700 San Martin Drive, Baltimore, MD 21218, USA.

<sup>3</sup>David A. Dunlap Department of Astronomy and Astrophysics, University of Toronto, 50 St. George Street, Toronto, Ontario, M5S 3H4, Canada.

<sup>4</sup>Dunlap Institute for Astronomy and Astrophysics, 50 St. George Street, Toronto, Ontario, M5S 3H4, Canada.

<sup>5</sup>Department of Astronomy, University of Texas at Austin, 2515 Speedway, Stop C1400, Austin, TX 78712, USA.

<sup>6</sup>Cosmic Frontier Center, The University of Texas at Austin, Austin, TX 78712.

<sup>7</sup>Department of Physics, Ben-Gurion University of the Negev, P.O. Box 653, Beer-Sheva 8410501, Israel.

<sup>8</sup>National Astronomical Observatory of Japan, National Institutes of Natural Sciences, 2-21-1 Osawa, Mitaka, Tokyo 181-8588, Japan.

<sup>9</sup>Graduate Institute for Advanced Studies, SOKENDAI, 2-21-1 Osawa, Mitaka, Tokyo 181-8588, Japan.

<sup>10</sup>School of Physics and Astronomy, Monash University, Clayton, VIC 3800, Australia.

<sup>11</sup>Department of Physics and Astronomy and PITT PACC, University of Pittsburgh, Pittsburgh, PA 15260, USA.

<sup>12</sup>Faculty of Mathematics and Physics, University of Ljubljana, Jadranska ulica 19, SI-1000 Ljubljana, Slovenia.

<sup>13</sup>Department of Physics and Astronomy, University of California Davis, 1 Shields Avenue, Davis, CA 95616, USA.

<sup>14</sup>Cosmic Dawn Center (DAWN), Niels Bohr Institute, University of Copenhagen, Jagtvej 128, DK2200 Copenhagen N, Denmark.

<sup>15</sup>Department of Physics, 60 St George St, University of Toronto, Toronto, ON M5S 3H8, Canada.

<sup>16</sup>Canadian Institute for Theoretical Astrophysics, 60 St George St, University of Toronto, Toronto, ON M5S 3H8, Canada.

<sup>17</sup>Institute for Cosmic Ray Research, The University of Tokyo, 5-1-5 Kashiwanoha, Kashiwa, Chiba 277-8582, Japan.

<sup>18</sup>Department of Physics, Graduate School of Science, The University of Tokyo, 7-3-1 Hongo, Bunkyo, Tokyo 113-0033, Japan.

<sup>19</sup>Kavli Institute for the Physics and Mathematics of the Universe (WPI), The University of Tokyo Institutes for Advanced Study, The University of Tokyo, Kashiwa, Chiba 277-8583, Japan.

<sup>20</sup>Department of Physics and Astronomy, Tufts University, 574 Boston Avenue, Suite 304, Medford, MA 02155, USA.

<sup>21</sup>Department of Astronomy and Mount Laguna Observatory San Diego State University, San Diego, CA 92182, USA.

<sup>22</sup>Univ Lyon, Univ Lyon1, Ens de Lyon, CNRS, Centre de Recherche Astrophysique de Lyon  
UMR5574, 69230, Saint-Genis-Laval, France.

<sup>23</sup>Center for Astrophysics | Harvard & Smithsonian, 60 Garden St., Cambridge, MA 02138, USA.

<sup>24</sup>Department of Physics & Astronomy, University of California, Los Angeles, 430 Portola Plaza,  
Los Angeles, CA 90095, USA.

<sup>25</sup>Department of Astronomy, Indiana University, 727 East Third Street, Bloomington, IN 47405, USA.

<sup>26</sup>Department of Astronomy, University of Illinois Urbana-Champaign, 1002 West Green Street, Urbana, IL 61801, USA.

<sup>27</sup>Instituto de Astrofísica de Andalucía (CSIC), Apartado 3004, 18080 Granada, Spain.

<sup>28</sup>European Southern Observatory, Alonso de Córdova 3107, Vitacura, Casilla 19001, Santiago, Chile.

<sup>29</sup>Institut d’Astrophysique de Paris, CNRS, Sorbonne Université, 98bis Boulevard Arago, 75014, Paris, France.

<sup>30</sup>Instituto de Alta Investigación, Universidad de Tarapacá, Casilla 7D, Arica, 1010000, Chile.

<sup>31</sup>Center for Astrophysics and Cosmology, University of Nova Gorica, Vipavska 11c, 5270 Ajdovščina, Slovenia.

<sup>32</sup>Jodrell Bank Centre for Astrophysics, University of Manchester, Oxford Road, Manchester, UK.

<sup>33</sup>Steward Observatory, University of Arizona, 933 N. Cherry Avenue, Tucson, AZ 85721, USA.

<sup>34</sup>Kapteyn Astronomical Institute, University of Groningen, P.O. Box 800, 9700AV Groningen, The Netherlands.

<sup>35</sup>School of Physics & Astronomy and Institute of Gravitational Wave Astronomy, University of Birmingham, UK.

<sup>36</sup>Instituto de Física de Cantabria (CSIC-UC). Avda. Los Castros s/n. 39005 Santander, Spain.

<sup>37</sup>IPAC, California Institute of Technology, 1200 E. California Blvd. Pasadena, CA 91125, USA.

<sup>38</sup>Kavli Institute for Astronomy and Astrophysics, Peking University, Beijing 100871, China.

<sup>39</sup>Department of Physics and Astronomy, Rutgers, the State University of New Jersey,  
Piscataway, New Jersey 08854, USA.

<sup>40</sup>Observatório Nacional, Rua General José Cristino, 77 - Bairro Imperial de São Cristóvão,  
Rio de Janeiro, 20921-400, Brazil.

<sup>41</sup>Laboratory for Multiwavelength Astrophysics, School of Physics and Astronomy, Rochester Institute of Technology,  
84 Lomb Memorial Drive, Rochester, NY 14623, USA.

<sup>42</sup>School of Physics & Astronomy, University of Minnesota, 116 Church St. SE, Minneapolis, MN 55455.

<sup>43</sup>Center for Interdisciplinary Exploration and Research in Astrophysics (CIERA),  
1800 Sherman Ave., Evanston, IL 60201, USA.

<sup>44</sup>School of Physical and Chemical Sciences — Te Kura Matū, University of Canterbury, Private Bag 4800,  
Christchurch 8140, Aotearoa, New Zealand.

<sup>45</sup>Centre for Astrophysics and Supercomputing, Swinburne University of Technology, Melbourne, VIC 3122, Australia.

<sup>46</sup>Observatório do Valongo, Universidade Federal do Rio de Janeiro,  
Ladeira do Pedro Antônio 43, Rio de Janeiro RJ 20080-090, Brazil.

<sup>47</sup>DTU-Space, Technical University of Denmark, Elektrovej 327, 2800, Kgs. Lyngby, Denmark.

<sup>48</sup>Institute of Science and Technology Austria (ISTA), Am Campus 1, 3400 Klosterneuburg, Austria.

<sup>49</sup>Department of Physics, Indian Institute of Science, Bengaluru 560012, India.

<sup>50</sup>MIT Kavli Institute for Astrophysics and Space Research, 70 Vassar Street, Cambridge, MA 02139, USA.

<sup>51</sup>Center for Frontier Science, Chiba University, 1-33 Yayoi-cho, Inage-ku, Chiba 263-8522, Japan.

<sup>52</sup>Department of Physics, Graduate School of Science, Chiba University, 1-33 Yayoi-Cho, Inage-Ku,  
Chiba 263-8522, Japan.

<sup>53</sup>Department of Astronomy, University of Maryland, College Park, 20742, USA.

<sup>54</sup>Département d'Astronomie, Université de Genève, Chemin Pegasi 51, 1290 Versoix, Switzerland.

<sup>55</sup>Finnish Centre for Astronomy with ESO (FINCA), Quantum, Vesilinnantie 5, University of Turku, FI-20014 Turku, Finland.

<sup>56</sup>Department of Physics, University of Helsinki, Gustaf Hällströmin katu 2, 00560 Helsinki, Finland.

<sup>57</sup>INAF – IASF Milano, via A. Corti 12, I-20133 Milano, Italy.

<sup>58</sup>Institute of Astronomy, Graduate School of Science, The University of Tokyo, 2-21-1 Osawa, Mitaka, Tokyo 181-0015, Japan.

<sup>59</sup>INAF-OAS, Osservatorio di Astrofisica e Scienza dello Spazio di Bologna, via Gobetti 93/3, I-40129 Bologna, Italy.

<sup>60</sup>University of California, Santa Cruz, 1156 High St., Santa Cruz, CA 95064, USA.

<sup>61</sup>School of Earth and Space Exploration, Arizona State University, Tempe, AZ 85287-6004, USA.

<sup>62</sup>Department of Natural Sciences, The Open University of Israel, Ra'anana 4353701, Israel.

<sup>63</sup>Astrophysics Research Center of the Open University (ARCO), Ra'anana 4353701, Israel.

\*Corresponding authors. Email: dcoulter@stsci.edu & clarison@stsci.edu

†These authors contributed equally to this work.

**We present the *JWST* discovery of “SN Eos”: a strongly lensed, multiply-imaged, SN II at a spectroscopic redshift of  $z = 5.133 \pm 0.001$ . SN Eos exploded when the Universe was only  $\sim 1$  billion years old, shortly after it reionized and became transparent to ultraviolet radiation. Archival *HST* imaging of SN Eos reveals rest-frame far ultraviolet ( $\sim 1,300$  Å) emission, indicative of shock breakout or interaction with circumstellar material in the first few (rest-frame) days after explosion. Follow-up *JWST* spectroscopy of SN Eos, now the farthest spectroscopically confirmed SN ever discovered, shows that SN Eos’s progenitor star likely formed in a metal-poor environment ( $\lesssim 0.1 Z_{\odot}$ ), providing strong, independent, and direct evidence for the chemical evolution of the Universe.**

Beginning 400 – 500 Myrs after the Big Bang, the neutral hydrogen that constituted the majority of the Universe underwent a phase transition driven primarily by ionizing UV radiation from small, intensely star-forming galaxies. This transition, which appears to have ended by  $z \approx 5.3$  (1), is referred to as the Epoch of Reionization [EoR, (2, 3)]. Direct observations of individual stars that existed during this early period would allow us to answer key questions about this phase in the Universe, such as how early stars formed the elemental building blocks of life, distributed these nucleosynthetic products to their surrounding ISM, and impacted their environment through stellar winds and ionizing radiation (4). Due to their extreme distances, the opportunities to study such stars remain quite limited (5). However, the explosive deaths of massive stars as core-collapse supernovae (CC SNe), which can be brighter than the total emission of their host galaxies, allow us to probe the final stages of stellar evolution. CC SN observations also reveal how heavy elements from stellar and SN nucleosynthesis, as well as unburnt elements that have been stored since the progenitor’s birth, are ejected into the environment. These early SNe are likely to be formed in lower metallicity environments than in the local Universe (6), and thus could have stellar progenitors more representative of the first generation of stars than their local counterparts (7). In-depth studies of early-Universe SNe therefore provide crucial data to constrain early stellar evolution models, the interplay between SN properties and their host conditions, the cosmic star formation rate, and the potentially evolving initial mass function (8).

To detect these extremely distant objects, the Vast Exploration for Nascent, Unexplored Sources [VENUS, (9)] *JWST* treasury program targets clusters of galaxies that act as gravitational telescopes, dramatically boosting the apparent brightness of distant sources and therefore opening a window to SNe in the infant Universe (10). This “strong” lensing effect leads to the appearance of multiple magnified images of the background object, each with a different arrival time to the observer. The difference between these arrival times is known as the “time delay” and depends on the distances to the components of the lens system, thus directly probing cosmological evolution [e.g, the Hubble constant, (11, 12)]. The magnification effect, which can reach a factor of ten to hundreds – or even thousands for rare sources near the thin regions of infinite magnification known as the “critical curves” (13, 14) – provides the ability to detect distant sources, such as SNe and galaxies, that would have otherwise been too faint to discover. Detailed analyses of rare objects that leverage this increase in signal, such as lensed stars and explosive transients, can shed light on early-Universe

physics (15–17).

## 1 Discovery of SN Eos

Here we present “SN Eos”, a multiply-imaged, strongly lensed transient discovered as a pair of images observed on 2025 September 1 (all dates presented are UTC) by VENUS in *JWST*/NIRCam imaging of the MACS 1931.8-2635 [ $z = 0.35$ ; (18)] galaxy cluster field (see Figure 1). Follow-up NIRCam imaging and NIRSpec PRISM spectroscopy of SN Eos taken on 2025 October 8 (*JWST* DDT PID: 9493, see Figure 2) reveal SN Eos to be a hydrogen-rich, core-collapse supernova (SN II) based on the clear detection of the hydrogen Balmer P-Cygni profiles. After the initial *JWST* discovery, an archival search of *Hubble Space Telescope* (*HST*) imaging of the cluster field reveals a non-detection of SN Eos, or its host, at these locations 13 years prior in 2012 to a  $5\sigma$  limiting magnitude of 27.3 AB mag in the WFC3/F814W and F110W filters. Repeat *HST* imaging of this field on 2024 March 11 – 18 show  $\sim 10\sigma$  ( $\sim 25\sigma$ ) detections in F814W [F110W; see table S1 in the Supplementary Text] on each of four (five) epochs over the course of this observer-frame week. At this redshift, the *HST* photometry corresponds to rest-frame far ultraviolet (FUV:  $\sim 1300 – 1900 \text{ \AA}$ ). A further archival search of data at the location of SN Eos from the Very Large Telescope (VLT) Multi Unit Spectroscopic Explorer (MUSE), taken in 2015 June [prior to the SN explosion, (18)], displays an isolated  $\lambda 7456 \text{ \AA}$  emission line (rest-frame  $1215 \text{ \AA}$ ) associated with Lyman- $\alpha$  (Ly $\alpha$ ) from the underlying host galaxy (Figure 3). Fitting for the redshift with this line, we find  $z_{spec} = 5.133 \pm 0.001$ , which clearly aligns with the emission line peaks in the SN Eos spectra.

## 2 Lens Model Description

Our lens model for MACS 1931.8-2635, described in more detail in (19), yields five predicted images for the SN Eos + host system (101.1-5). In two of these predicted images, 101.1-2, SN Eos is detected in *JWST*/NIRCam observations (see table S1 in the Supplementary Text). In predicted images 101.3-4, strong Ly $\alpha$  emission from the host galaxy was detected in pre-explosion MUSE data, while the fifth predicted image, 101.5, was not covered by the archival MUSE image footprint [see (19)]. As a result of the close proximity to the critical curve, images 101.1-2 are highly magnified (by factors of  $\mu_{101.1} \approx 25.46 \pm 5.73$  and  $\mu_{101.2} \approx 29.88 \pm 6.22$ ) and have a short, observer-frame

predicted time delay of  $\sim 1$  day between them ( $\sim 4$  rest-frame hours), with image 101.2 being the last to arrive. SN Eos was not detected in the other three locations; the model predicts that the light from SN Eos arrived years earlier and was not as highly magnified. We summarize the magnification and time delays computed using the cluster lens model in table S2 in the Supplementary Text, and throughout use a standard flat  $\Lambda$ CDM cosmology with  $H_0 = 70 \text{ km s}^{-1} \text{ Mpc}^{-1}$ ,  $\Omega_\Lambda = 0.7$ , and  $\Omega_m = 0.3$ .

### 3 Spectrophotometric Classification

Figure 2 shows the spectroscopic observations of the two detected images (101.1 and 101.2) of SN Eos, taken 94 rest-frame days after the archival *HST* detections, which show a clear identification of the hydrogen Balmer lines, specifically  $\text{H}\alpha$ ,  $\text{H}\beta$ ,  $\text{H}\gamma$ , and  $\text{H}\delta$ . These all show P-Cygni profile shapes that are characteristic of SNe, which consist of a blueshifted absorption component in addition to the emission line, and we unambiguously classify SN Eos as a Type II supernova (SN II). We further note the presence of other common SN II elemental species, namely oxygen, sodium, and calcium. As shown in the top-left panel of Figure 2, most of the commonly shared features between the spectra of the two images appear nearly identical, consistent with the small predicted time delay [see table S2 in the Supplementary Text, as well as (19) for a detailed discussion].

We further classify SN Eos’ SN subtype by considering its early UV light curve. In SNe II, far-UV (FUV) radiation at the brightness we see in SN Eos may be emitted within the first few days of explosion and is thus rarely detected. Generally, SNe II FUV light curves rise within  $\sim 2 - 5$  days of explosion and then rapidly fade due to the SN ejecta expanding and cooling (20–22). The presence of strong FUV radiation in the archival *HST* imaging therefore points to the detection of SN Eos within a few rest-frame days of explosion. Due to a lack of a constraining non-detection, however, we conservatively fix the explosion time,  $t_0$ , of SN Eos to within five rest-frame days before the first *HST* detection. Combined with the redshift, this places our *JWST* observations at approximate phases of  $\sim 92$  and  $\sim 98$  rest-frame days post-explosion. For SNe II progenitors that retain massive hydrogen-rich envelopes, hydrogen recombination powers a relatively constant luminosity and results in a  $\sim 50 - 100$  rest-frame day “plateau” (23), after which heating by the radioactive decay of  $^{56}\text{Co}$  and other long-lived radioactive elements becomes the primary source of luminosity. As further described in (19), we compare our measured (demagnified) photometry to a

grid of low-metallicity red supergiant (RSG) SN progenitor models, and conclude that SN Eos is consistent with a SN IIP at the end of its plateau phase – as constrained by the UV detection.

## 4 Host Galaxy Analysis

Apart from the aforementioned strong Ly $\alpha$  line (Figure 3), the host of SN Eos is faint and only marginally detected in the stacked rest-UV NIRCam images (F090W, F115W, and F150W), subtended by an angular length of  $\sim 0.4''$  and width of  $\sim 0.1''$ . These detections lead to an apparent rest-UV magnitude of  $28.5 \pm 0.4$  AB mag for system 101.2, which corresponds to  $M_{\text{UV}} \approx -14.4$  AB mag after correcting for magnification, line-of-sight Milky Way dust extinction (24, 25), and applying the redshift-dependent  $K$ -correction (26). Given this combination, we identify the host of SN Eos to be a Lyman- $\alpha$  emitter (LAE) galaxy, which are faint and metal-poor galaxies with high specific star formation rates at high- $z$  (27). According to the mass-metallicity relationship (MZR), fainter, lower-mass galaxies should have lower (gas-phase) metallicity. The fact that other high-redshift, low-mass galaxies and emitting regions observed with *JWST* follow this relationship and are found to have  $Z \lesssim 0.1 Z_{\odot}$  (28–30) provides supporting evidence that the gas-phase metallicity of the host of SN Eos, and thus the underlying environment of SN Eos, is also  $< 0.1 Z_{\odot}$ . Therefore, by leveraging strong lensing, our observations are probing the fainter (and lower metallicity) end of the LAE UV luminosity function compared to *JWST* blank deep field surveys [e.g., (27, 31)]. Given the singular MUSE detection of the Ly $\alpha$  line at a low significance (and lack of any other identifying lines), this LAE would not have been identified without the presence of SN Eos, suggesting that high- $z$  CC SNe could help reveal a population of star-forming galaxies that are otherwise incredibly difficult to detect.

## 5 Low- $z$ Comparison and Light Curve Modeling

Given our extremely high signal-to-noise spectrum, SN Eos provides a rare opportunity to directly test the inferred low metallicity of its LAE host. It has been predicted that because red supergiant (RSG) envelopes should be only weakly affected by nuclear burning, the presence of Fe-group elements in the hydrogen-rich envelope at late times is representative of the metallicity of the gas out of which the stellar progenitor formed (8, 32, 33), thereby motivating their use as metallicity

probes of the Universe. This prediction was supported by (34–36) in the local Universe, finding a positive correlation with the strength of metal lines observed in SNe IIP spectra and the metallicity inferred from local measurements of the host HII regions. By combining each lens image spectrum of SN Eos, we have the first opportunity to measure the “pseudo-equivalent” width (pEW) of Fe II  $\lambda 5018, 5169 \text{ \AA}$  in an SN IIP near the EoR. We show in Figure 2 an overlay of strong- and weak-Fe features in local SNe IIP, and notably contrast SN Eos’ Fe II complex with known local, low-metallicity SNe 2015bs (37), SN 2017ivv (38), and SN 2023ufx (39, 40). This shows that the pEWs of SN Eos are closely matched to these rare,  $\lesssim 0.1 Z_{\odot}$  examples.

We provide context for this measurement in Figure 4 which follows the evolution of pEW Fe II  $\lambda 5018 \text{ \AA}$  as a function of rest-frame SN phase. Overlaid are SNe II data from (34) along with spectral models as a function of metallicity from (33). We caution that because our SN phase constraints from *HST* place our spectral observations at  $\sim 98$  days, SN Eos’ photosphere would be cooler than most of those measured by (34), and therefore our measurement would appear deeper/higher metallicity than if it had been measured at an earlier phase. Therefore, we take our inferred metallicity from this measurement as an upper limit consistent with  $Z \lesssim 0.1 Z_{\odot}$ , in agreement with an order estimate of the metallicity expected from the ultra-faintness of the host and placing SN Eos in the small class of known, extremely metal-poor SNe IIP.

We further model SN Eos by fitting a series of self-consistent, hydrodynamical models to our *HST* and *JWST* photometry. We note, however, that the model fit is highly sensitive to the absolute luminosity and light curve shape of SN Eos, and therefore to the lens model magnifications and time delays [see (19)]. To minimize biasing the fit by the uncertainties in the lens model, we select only the brighter lens image to fit (101.2, with  $\mu \sim 30\times$ ), calculate a distance modulus  $\mu_{DM} \approx 46.4$  AB mag, and combine  $\mu$  and  $\mu_{DM}$  with several lens-independent observational constraints (e.g., the time of explosion,  $t_0$ , the apparent decline in the plateau, and inferred metallicity of  $\lesssim 0.1 Z_{\odot}$ ) to produce the model fits displayed in Figure 5. Because it is possible that future lens models may produce differing magnifications for lens image 101.1 and 101.2, we simply present our observed photometry for lensed images 101.1 and 101.2 in table S1 in the Supplementary Text. We report that our best models are of a typical SN IIP (in mass and explosion energy) with a slightly more luminous *B*-band peak than the average SN IIP [ $-17.7$  AB mag vs.  $\bar{M}_B = -16.80 \pm 0.37$  AB mag; (41)], with two different prescriptions for  $^{56}\text{Ni}$  mixing, and a spherical shell of confined CSM that relates

the early rest-frame UV data to our rest-frame optical observations at  $\sim +98$  days. In the left panel of Figure 5 we zoom in on this early UV light curve and note that there is unaccounted for UV flux in the first two epochs that could be consistent with a more complex interaction scenario. Despite this, our simplified model is consistent with the subsequent UV rise and relative luminosity of the *HST* F110W and F814W photometry. A detailed description of this modeling process, our best-fit model, and our treatment of the UV light curve is presented in (19).

As shown in Figure 2, it is clear that SN Eos shares several properties with both low- and high-metallicity SNe. SN Eos best matches the spectral features of the solar-metallicity SN 1992H, especially in its  $\text{H}\alpha$  and  $\text{Na I}$  profiles. However, it is clear that SN Eos’ Fe II complex better matches that of SN 2015bs, SN 2017ivv, and SN 2023ufx, the only local SNe II with very low metallicity. In (19) we provide a more detailed comparison between SN Eos and these local SNe, but we note that SN Eos also better matches the three low- $Z$  SNe in terms of SN Eos’ inferred luminosity, host galaxy mass, and host metallicity. Surprisingly, even for SNe II of similar, very low metallicities, there is a large diversity in their spectral and photometric properties (23, 42, 43). It has been speculated that this dispersion in properties arises from the detailed physics of each individual explosion, and that factors ranging from the size and structure of the progenitor star, its mass-loss history, rotation, and existence of a binary companion can have non-trivial and degenerate effects on SN observables; e.g., peak luminosities, plateau durations, or the strength and shape of spectral features (33, 44, 45). With our relatively small data set, we cannot confidently infer the progenitor properties of SN Eos, and assessing whether or not low-redshift, low- $Z$  SNe are true analogs to their early-Universe counterparts is still an open question. Despite this, our combined spectrum of SN Eos presents the first genuine test of these analogs, and based on how “typical” SN Eos appears, also supports the results of (34) — that metallicity alone is not strongly correlated with any spectrophotometric SN property other than the pEW of Fe II. A definitive answer to this question will require the discovery of many more high-redshift and local, low- $Z$  SNe, with well-sampled light curves and spectra. Such a sample would allow for self-consistently modeling the entire population as done by (23, 46–48), providing statistically robust measurements of SN progenitor and explosion properties as a function of redshift and metallicity. Furthermore, calibrating these SNe II as metallicity probes would allow for a constraint on the rate of chemical enrichment as a function of redshift and host galaxy properties – especially for incredibly faint galaxies – informing the evolution of the MZR (49).

## 6 Implications for Future High-redshift Studies

The discovery of SN Eos, a strongly-lensed, multiply-imaged, and highly-magnified SN II at  $z = 5.133 \pm 0.001$  embedded in a very faint, LAE host galaxy, has allowed us for the first time to compare SNe in the local Universe to a SN close to the EoR. With an exquisite, high signal-to-noise follow-up NIRSpec spectrum rivaling the spectra taken of local SNe, we can unambiguously classify SN Eos and probe the physics of its explosion. Our spectrum reveals weak absorption of Fe II  $\lambda 5018, 5169$  Å, a known tracer of the gas-phase metallicity of the SN environment, and extends the use of SNe II as metallicity tracers to the early Universe. Our measurement confirms that SN Eos exploded in an environment with a metal concentration  $\lesssim 10\%$  that of the solar abundance. In the local Universe, these low-metallicity SNe are incredibly rare ( $<< 1\%$  of all SNe II); the fact that the *first* SN II at  $z > 5$  with a high enough fidelity spectrum to directly assess its metallicity has such a low value is itself strong, independent, and direct evidence for the chemical evolution of the Universe. Serendipitous *HST* observations, prior to the *JWST* discovery, show that in the rest-frame, SN Eos had variable, bright, and rising FUV emission. We model this early UV light curve to emission occurring just days after explosion, and posit that a secondary rise in the UV is consistent with a moderate amount of confined, circumstellar material around the progenitor star. We compare SN Eos to local examples of SNe II, focusing on both the best, low-metallicity examples in the literature, as well as our best spectral match at solar-metallicity, and find that SN Eos shares similarities with both sets of SNe. Finally, we emphasize that because SNe II arise from deaths of massive stars, their progenitors have short lifetimes and trace the instantaneous star formation rates of their hosts. Integrating SN II follow-up observations in high- $z$  galaxy surveys can therefore provide a more unbiased way of studying the faint end of the galaxy luminosity function compared with methods that assume a model (50). Our results demonstrate that by leveraging the magnification afforded by gravitational lensing surveys, we have opened a new frontier in precision, high-redshift transient science. The discovery of SN Eos represents a critical step toward fulfilling *JWST*'s core mission objectives of understanding the lives and deaths of the first stars, the origins of the elements, and the assembly and evolution of the youngest galaxies.

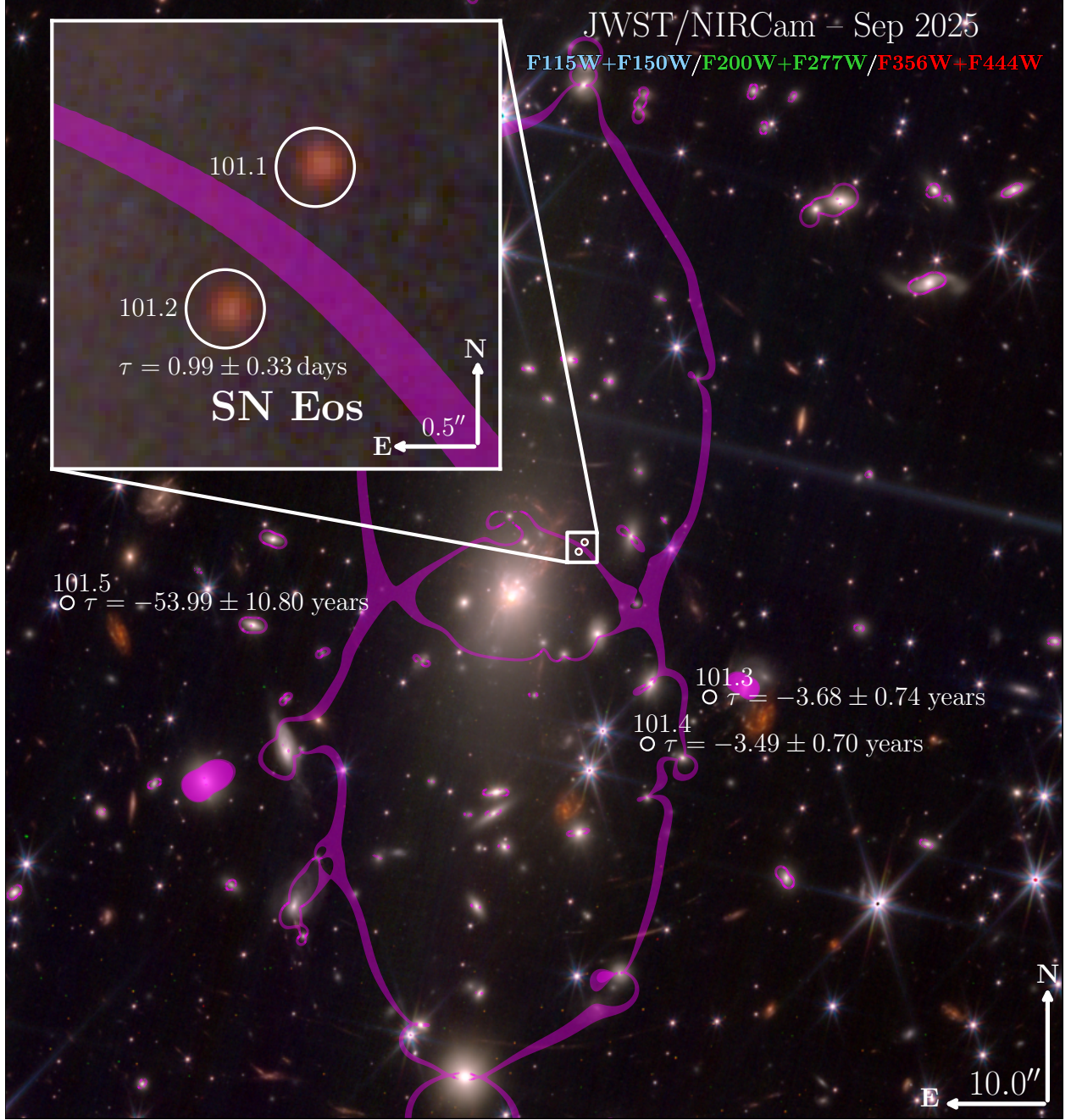


**Figure 1: JWST discovery image of the MACS 1931.8-2635 galaxy cluster containing SN Eos.** The RGB color channels are as follows: blue [F115W + F150W], green [F200W + F277W], and red [F356W + F444W]. The magenta shaded area corresponds to a region where the model-predicted magnification is  $\mu > 100$  at  $z = 5.133 \pm 0.001$ . The upper left inset shows the two detected images of SN Eos, 101.1 & 101.2, mirrored by the critical curve, which represents the thin region of infinite magnification in the lens system for the source redshift. The proximity of these images to the critical curve results in a high magnification, predicted to be  $\sim 30$  at the image 101.1/101.2 positions. In the main image (outside the inset), we display the predicted positions and time delays,  $\tau$ , of images 101.3, 101.4, and 101.5. The angular scales are labeled on the N-E orientation arrows.

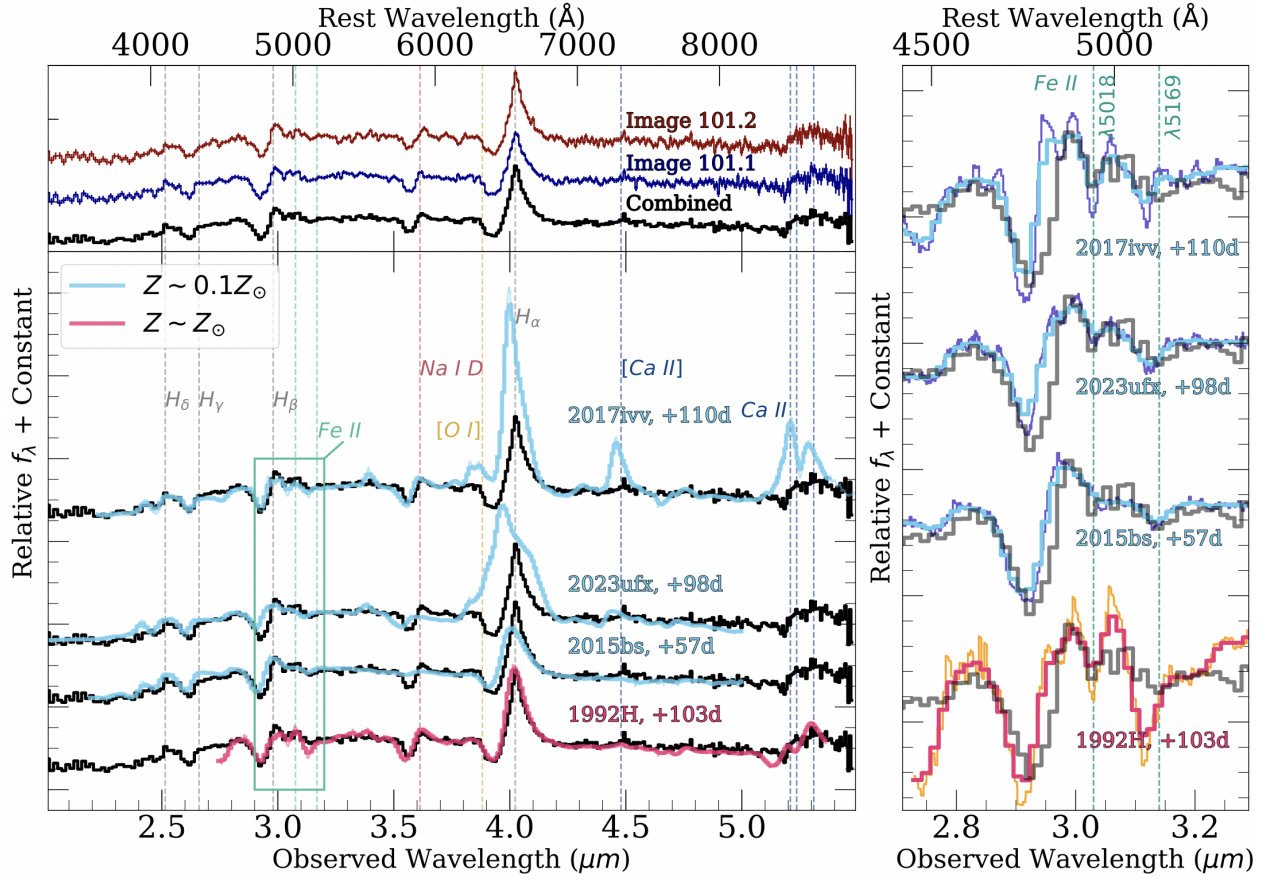


**Figure 2: Comparison of NIRSec PRISM spectra taken of SN Eos (top-left) to local SNe IIP (bottom-left) and comparisons of the Fe line profiles (right) of these same objects..** *Top Left:* In red and blue, spectra of individual lensed images of SN Eos are overlaid, demonstrating that each lens image shows the same SN at a similar phase. The inverse-variance weighted combined spectrum is shown in black and used in comparisons below. *Bottom Left:* Comparisons of our combined spectrum to the optical spectra of local SNe IIP, normalized to their continua, convolved and resampled with the *JWST* NIRSpec PRISM dispersion function. Spectra overlaid in blue are a sample of known, well-studied SNe II with metallicities consistent with  $Z \lesssim 0.1 Z_{\odot}$ : SN 2017ivv (38), SN 2023ufx (39, 40), and SN 2015bs (37). The overlaid spectrum in red corresponds to the best-matching local SN II, SN 1992H at  $\sim 1 Z_{\odot}$  [see (19) for discussion of matching procedure]. These comparisons demonstrate that SNe IIP display many similarities despite having a range of metallicities, and even for SNe IIP with similar metallicities there is still an intrinsic diversity in spectral features. This is consistent with findings from (34) which claim that metallicity alone is not strongly correlated with all spectral observables. *Right:* A detailed view of the Fe II complex for the same SNe, with SN Eos in gray. Each local SN has its native spectral resolution (purple and orange) and NIRSpec PRISM-convolved resolution (blue and red) overplotted onto SN Eos.

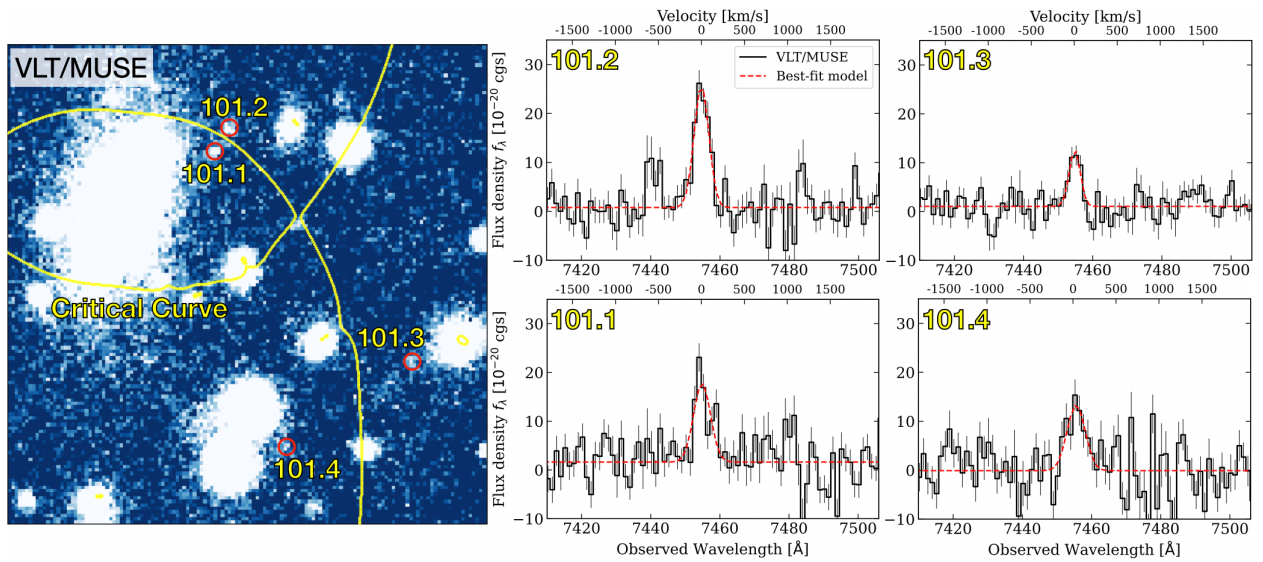


**Figure 3: VLT/MUSE observations of the SN Eos host galaxy.** *Left:* the moment-zero map centered on the narrow wavelength range of  $\lambda_{\text{obs}} = 7452 \text{ \AA}$  to  $7458 \text{ \AA}$ , generated from MUSE data cube. Multiple images of the system (image 101.1, 101.2, 101.3, and 101.4) are detected. *Right:* VLT/MUSE spectra extracted at the positions of multiple images. The Ly $\alpha$  lines are detected at  $\lambda_{\text{obs}} = 7455 \text{ \AA}$  in all images, with a measured redshift of  $z = 5.133 \pm 0.001$ . The best-fit single Gaussian profiles are shown in red.

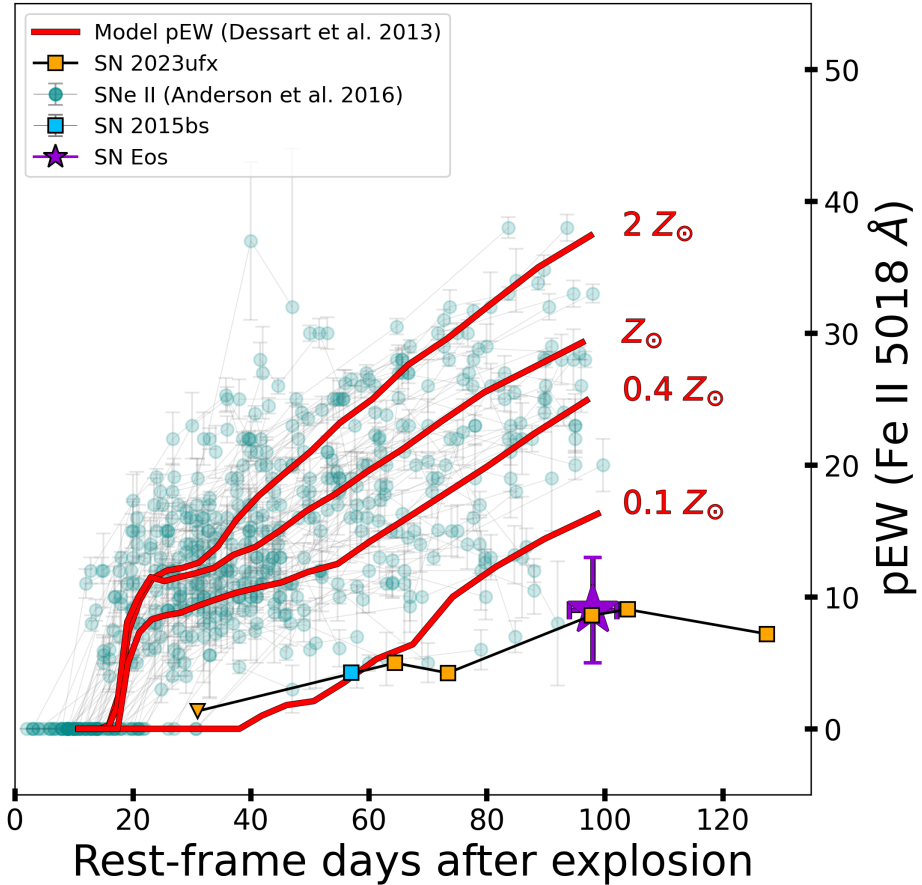


**Figure 4: The evolution of pEW Fe II  $\lambda 5018 \text{ \AA}$  measured in local SNe IIP as a function of SN phase.** In teal are SNe data from (34) with errors, and overlaid in red are spectral models as a function of metallicity from (33). SN Eos is shown as a purple star, with SN 2023ufx as orange squares, with the inverted triangle as a pEW upper limit (39). A single measurement for SN 2015bs is plotted as a blue square (37). Our measurement, along with the inferred phase, places SN Eos in a likely parameter space that is  $Z \lesssim 0.1 Z_{\odot}$ .

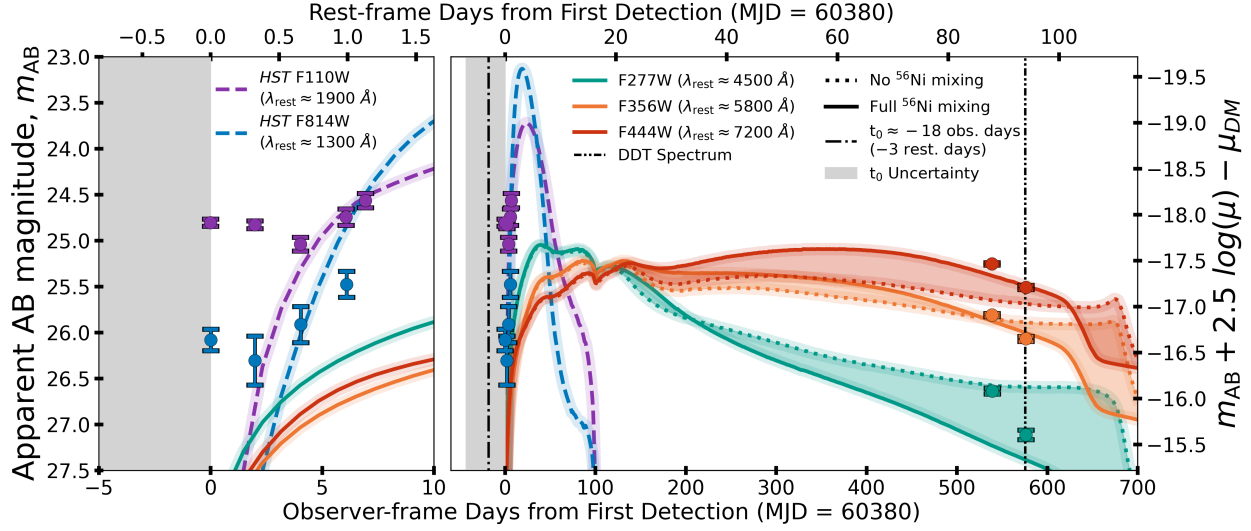


**Figure 5: Light curve of SN Eos, highlighting early FUV detections, with comparison against a theoretical model.** *Right:* *HST* and *JWST* photometry for lens image 101.2, the higher signal-to-noise image, in case of a phase difference between 101.1 and 101.2 (see table S2 in the Supplementary Text). Overplotted are in-band light curves from the modeling in (19), placing our *JWST* observations at the end of an SN IIP’s plateau. The *HST* data were obtained as 4 – 5 epochs over an observer-frame week, and are assumed to be near-explosion. The gray region marks the assumed window for  $t_0$ , the time of explosion, that we constrain to  $\lesssim 5$  rest-frame days from the first *HST* detection (see main text). *Left:* A zoomed-in view of the same *HST* F110W and F814W photometry, showing the variability of SN Eos on a rest-frame  $\sim 1$  day timescale. The model prediction, containing a moderate amount of CSM material, is in rough agreement with the later luminosity and evolution of this UV emission, however, we note that the first 2 epochs in F814W and F1101W are in excess of this simple CSM model suggesting that this flux could be due to more complicated effects, e.g., asymmetric structure in the confined CSM [see (19)].

## Acknowledgments

**Funding:** We acknowledge the support of the Canadian Space Agency (CSA) [25JWGO4A18]. Numerical computations were in part carried out on a PC cluster at the Center for Computational Astrophysics, National Astronomical Observatory of Japan. This work is based on observations made with the NASA/ESA/CSA James Webb Space Telescope. The data were obtained from the Mikulski Archive for Space Telescopes at the Space Telescope Science Institute, which is operated by the Association of Universities for Research in Astronomy, Inc., under NASA contract NAS 5-03127 for JWST. These observations are associated with JWST PID 6882. Support for PID 6882 was provided by NASA through a grant from the Space Telescope Science Institute. The authors acknowledge the use of the Canadian Advanced Network for Astronomy Research (CANFAR) Science Platform operated by the Canadian Astronomy Data Center (CADC) and the Digital Research Alliance of Canada (DRAC), with support from the National Research Council of Canada (NRC), the Canadian Space Agency (CSA), CANARIE, and the Canadian Foundation for Innovation (CFI).

C.L. and D.A.C. acknowledge funding through *JWST* program grants JWST-GO-06541, JWST-GO-06585, and JWST-GO-05324. R.A. acknowledges support of Grant PID2023-147386NB-I00 funded by MICIU/AEI/10.13039/501100011033 and by ERDF/EU, and the Severo Ochoa award to the IAA-CSIC CEX2021-001131-S and from grant PID2022- 136598NB-C32 “Estallidos8”. H.A. acknowledges support from CNES, focused on the *JWST* mission, and the French National Research Agency (ANR) under grant ANR-21-CE31-0838. F.E.B. acknowledges support from ANID-Chile BASAL CATA FB210003, FONDECYT Regular 1241005, and ECOS-ANID ECOS240037. M.B. acknowledges support from the ERC Grant FIRSTLIGHT, Slovenian national research agency ARIS through grants N1-0238 and P1-0188, and ESA PRODEX Experiment Arrangement No. 4000149972. M.B. and T.P. acknowledge the financial support from the Slovenian Research Agency (grants I0-0033, P1-0031, J1-8136, J1-2460, Z1-1853 and N1-0344) and the Young Researchers program, as well as the financial support from European Space Agency PRODEX Experiment Arrangement EArTH. C.J.C. acknowledges support from the ERC Advanced Investigator Grant EPOCHS (788113). P.D. warmly acknowledges support from an NSERC discovery grant (RGPIN-2025-06182). S.D. is supported by UK Research and Innovation (UKRI) under the UK govern-

ment's Horizon Europe funding Guarantee EP/Z000475/1. J.M.D. acknowledges the support of projects PID2022-138896NB-C51 (MCIU/AEI/MINECO/FEDER, UE) Ministerio de Ciencia, Investigación y Universidades and SA101P24. P.L.K. acknowledges funding from STScI GO-17504 and NSF AAG 2308051. I.L. acknowledges support by the Australian Research Council through Future Fellowship FT220100798. Z.G.L. is supported by the Marsden Fund administered by the Royal Society of New Zealand, Te Apārangi grants M1255. X.L. is supported by an LSST-DA Catalyst Fellowship through the support of Grant 62192 from the John Templeton Foundation to LSST-DA. G.E.M. acknowledges the Villum Fonden research grants 37440 and 13160. N.M. acknowledges support from the ERC Grant FIRSTLIGHT and the Slovenian National Research Agency ARRS through grant N1-0238. G.N. acknowledges support by the Canadian Space Agency under a contract with NRC Herzberg Astronomy and Astrophysics. M.P. is supported by NASA through an Einstein Fellowship grant No. HST-HF2-51583.001-A awarded by the Space Telescope Science Institute (STScI), which is operated by the Association of Universities for Research in Astronomy, Inc., for NASA, under contract NAS5-26555. T.P. acknowledges the financial support for the bilateral collaboration between STScI and UNG (BI-US/24-26-085). M.R.S. is supported by an STScI Postdoctoral Fellowship. Q.W. is supported by the Sagol Weizmann-MIT Bridge Program. J.R.W. acknowledges that support for this work was provided by The Brinson Foundation through a Brinson Prize Fellowship grant. R.A.W. acknowledges support from NASA JWST Interdisciplinary Scientist grants NAG5-12460, NNX14AN10G and 80NSSC18K0200 from GSFC. Y.X. is supported by JSPS KAKENHI Grant Number JP25KJ1029. A.Z. acknowledges support by the Israel Science Foundation Grant No. 864/23.

**Author contributions:** D.A.C. and C.L. led the analysis of the main text and supplementary material, contributing to each figure and table. J.D.R.P. worked on the photometry of SN Eos, including work on Figures 5, S1 and Table S1. S.F. is the PI of VENUS and led coordination of analysis efforts for this work. V.K. led the data reduction process for the *JWST* and [HST] data used in this paper. J.F.V.A. constructed the lens model used in this paper, as well as contributed to the analysis of the MUSE dataset. T.J.M. worked on the light curve modelling of SN Eos, directly contributing to Figure 5. M.S. helped with the spectroscopic reduction of the *JWST* NIRSpec observations and contributed extensively to Figure 2. Y.A. contributed analysis of the host galaxy

of SN Eos and contributed to Figure 3. R.B. and M.B. provided insight into the interpretation of the lens model and physical nature of SN Eos. G.B. helped with both data reduction and analysis. J.C., D.C., P.D., M.E., S.L.F., O.D.F., L.J.F., A.M.K., T.M., M.N., M.O., R.P., R.Q., A.R., J.R., L.R., L.G.S., F.S., T.T., H.Y. are key members of the VENUS team who provided valuable insight into the SN and lens modeling analysis. A., A.A., R.A., J.P.A., R.A., H.A., F.E.B., L.D.B., V.B., M.B., C.J.C., C.D., J.M.D., G.D., S.D., J.M.D., E.E., A.F., B.F., S.G., M.G.-O., M.G., Y.H., K.I., S.W.J., Y.J.-T., J.S.K., P.L.K., L.A.K., Z.G.L., X.L., I.L., P.A.A.L., R.A.L., G.E.M., N.S.M., J.M., A.K.M., R.P.N., G.N., M.O., E.P.G., M.P., T.P., M.R., D.S., S.S., M.S., W.S., K.S., A.T., E.V., Q.W., J.W., R.W., R.W., Y.X., Y.Z., A.Z. provided valuable analysis into the lens modeling and SN physics interpretations of this article.

**Competing interests:** “There are no competing interests to declare.”

**Data and materials availability:** All *HST* and *JWST* data presented and analyzed in this article can be accessed here: <https://www.doi.org/10.17909/r2dr-mq75>. The MUSE data can be accessed via the European Southern Observatory archive: <https://tinyurl.com/muse-eos-data>.

# Supplementary Materials for

## A spectroscopically confirmed, strongly lensed, metal-poor Type II supernova at $z = 5.13$

David A. Coulter<sup>\*†</sup>, Conor Larison<sup>\*†</sup>, Justin D. R. Pierel, Seiji Fujimoto, Vasily Kokorev, Joseph F. V. Allingham, Takashi J. Moriya, Matthew Siebert, Yoshihisa Asada, Rachel Bezanson, Maruša Bradač, Gabriel Brammer, John Chisholm, Dan Coe, Pratika Dayal, Michael Engesser, Steven L. Finkelstein, Ori D. Fox, Lukas J. Furtak, Anton M. Koekemoer, Thomas Moore, Minami Nakane, Masami Ouchi, Richard Pan, Robert Quimby, Armin Rest, Johan Richard, Luke Robbins, Louis-Gregory Strolger, Fengwu Sun, Tommaso Treu, Hiroto Yanagisawa, Abdurro'uf, Aadya Agrawal, Ricardo Amorín, Joseph P. Anderson, Rodrigo Angulo, Hakim Atek, Franz E. Bauer, Larry D. Bradley, Volker Bromm, Mateusz Bronikowski, Christopher J. Conselice, Christa DeCoursey, James M. DerKacy, Guillaume Desprez, Suhail Dhawan, Jose M. Diego, Eiichi Egami, Andreas Faisst, Brenda Frye, Sebastian Gomez, Mauro González-Otero, Massimo Griggio, Yuichi Harikane, Kohei Inayoshi, Saurabh W. Jha, Yolanda Jiménez-Teja, Jeyhan S. Kartaltepe, Patrick L. Kelly, Lindsey A. Kwok, Zachary G. Lane, Xiaolong Li, Ivo Lobbe, Paulo A. A. Lopes, Ray A. Lucas, Georgios E. Magdis, Nicholas S. Martis, Jorryt Matthee, Ashish K. Meena, Rohan P. Naidu, Gaël Noirot, Masamune Oguri, Estefania Padilla Gonzalez, Massimo Pascale, Tanja Petrushevska, Massimo Ricotti, Daniel Schaerer, Stefan Schuldt, Melissa Shahbandeh, William Sheu, Koji Shukawa, Akiyoshi Tsujita, Eros Vanzella, Qinan Wang, John Weaver, Robert Williams, Rogier Windhorst, Yi Xu, Yossef Zenati, Adi Zitrin

<sup>\*</sup>Corresponding authors. Email: dcoulter@stsci.edu & clarison@stsci.edu

<sup>†</sup>These authors contributed equally to this work.

### This PDF file includes:

Materials and Methods

Figure S1

Tables S1 to S2

## Materials and Methods

### 6.1 JWST Discovery

SN Eos was discovered in *JWST* NIRCam imaging acquired on 2025 September 1 (all dates presented will be UTC), by the Vast Exploration for Nascent, Unexplored Sources collaboration [VENUS, (9)] in the MACS 1931.8-2635 [ $z = 0.35$ , (18)] galaxy cluster field. Observations of the cluster included 10 NIRCam filters: [short-wavelength (SW): F090W, F115W, F150W, F200W, F210M] and [long-wavelength (LW): F277W, F300M, F356W, F410M, F444W] and are part of the larger VENUS program to image  $\sim 60$  rich galaxy clusters with *JWST*. The VENUS image reduction process is as follows. We begin with *JWST* Level-2 MAST products and process them using the `grizli` pipeline (51), following the approach used in the public DJA reduction<sup>1</sup>. We use the CRDS context map `jwst_1456.pmap` for the photometric calibration. Compared to the standard STScI pipeline, `grizli` applies enhanced procedures to alleviate effects from cosmic rays, scattered light and detector artifacts (52, 53). We further perform additional background, 1/f noise and diffraction spike subtraction at both the amplifier and mosaic levels [e.g., (54, 55)]. Final NIRCam mosaics are then drizzled to native pixel scales for each detector (SW: 0.03''/pix, LW: 0.06''/pix).

### 6.2 HST Archival Detection

*Hubble Space Telescope (HST)* imaging of the cluster field reveals a clear early rest-frame far ultra-violet (FUV;  $\sim 1300 - 1900 \text{ \AA}$ ) detection of SN Eos. This imaging was acquired on 2024 March 11, 13, 15, 17, 18 as part of an *HST* SNAP survey program to identify lensed stars [PID: 17504, (56)] in the WFC3/UVIS F814W and WFC3/IR F110W filters. The total exposure times for these two filters on each day were, in chronological order and for F814W & F110W respectively, [(2220 s, 1068 s), (1110 s, 609 s), (1110 s, 459 s), (880 s, 369 s), (880 s, 369 s)]<sup>2</sup>. In a similar manner as for *JWST*, we process the *HST* data from the level 2 MAST products. For F814W, we use the products that include the pixel-based corrections for charge transfer efficiency (CTE). For

---

<sup>1</sup><https://dawn-cph.github.io/dja/>

<sup>2</sup>The fifth epoch of the WFC3/UVIS F814W data appears to have suffered a guide-star failure, and thus we do not include it in the analysis.

both filters and all epochs (table S1), we again drizzle exposures using the `grizli` pipeline (51), following the approach used in the public DJA reduction. We use the native pixel scales for these products as well, corresponding to  $0.04''/\text{pix}$  for F814W and  $0.13''/\text{pix}$  for F110W.

### 6.3 VLT MUSE Archival Detection

Further archival Very Large Telescope (VLT) Multi Unit Spectroscopic Explorer (MUSE) data was retrieved from the ESO data archive that was taken on 2015 June 12 and July 17 – as a series of six exposures, each of 1462 s – thus preceding the *JWST* observation of images 101.1-2 (see Main Text Figure 1) of SN Eos by over a decade, or around 20 rest-frame months [data and analysis presented in (18)]. The locations of the SN appear coincident with the detection of an isolated emission line that corresponds to Ly $\alpha$  emission and was previously unreported. These detections are at a significance of  $7.9\sigma$ ,  $12.0\sigma$ ,  $6.4\sigma$ , and  $5.8\sigma$  for images 101.1-4 respectively. Due to these data being taken well before the SN exploded in these images, this line is associated with the host galaxy of SN Eos and is also seen at two of the other host galaxy image locations (shown in Main Text Figure 3) . A further dedicated analysis on the properties of this host will be presented in Y. Asada et al. (*in prep.*).

### 6.4 JWST DDT Observations

Spectrophotometric observations with *JWST* were executed on 2025 October 8 (DDT PID: 9493, PI: Coulter). This included a NIRSpec PRISM/CLEAR spectroscopic observation of both visible images 101.1 and 101.2 (with 10,504 s of exposure each), as well as follow-up NIRCam imaging (with 805 s of exposure) in the F277W, F356W, and F444W bands, each paired with the F070W SW filter (in an attempt to detect the underlying host). The NIRCam imaging was reduced using the standard VENUS procedure outlined in Supplementary Text section 6.1, while the NIRSpec spectra were reduced using the tools included in the `msaexp` package (57).

### 6.5 Photometry

We use STARRED (58, 59) to measure *HST* photometry of SN Eos using the final drizzled products described in Supplementary Text section 6.1, which is a Python package for scene modeling PSF

photometry, optimized for light curve extraction. In STARRED, the background is modeled on a grid of pixels with half the pixel size of the original image and regularized using starlets (60). We use the template imaging (figure S1) to constrain this static background, and then STARRED takes as input all time-series images along with a PSF model for each epoch to measure the SN light curve. The PSF is reconstructed with STARRED for each filter and epoch using 8 non-saturated stars in the field of view, and then each *HST* band is processed independently.

STARRED does not perform well when there is no template imaging, as there is a degeneracy between the background reconstruction and the point source flux (61). Therefore for *JWST*, where no template exists, we rely on robust aperture photometry with 3 pixel radii, implemented on the final drizzled products, and background estimation using an annulus with inner and outer radii defined by the default reported aperture corrections (also applied to the raw measured fluxes) for each instrument. As all *HST* and *JWST* images were converted to the same units (10 nJy) by the *grizli* pipeline, all flux measurements were simply converted to AB magnitudes directly with the corresponding zero-point of 28.9. All measured photometry, including  $5\sigma$  upper-limits, are reported in table S1.

## 6.6 Lens Model

We construct a lens model for the galaxy cluster MACS 1931.8-2635 using a Python-implemented, updated version of the parametric method by [ (62), but see also (63, 64) where more details are provided]. The lens model and its implementation will be detailed in separate companion article (Allingham et al., in prep.), and here we summarize its main properties.

The lens model consists of a dark-matter component and a galaxy component. With the cluster appearing mostly relaxed, we model its dark-matter component with one large, smooth dark-matter halo, corresponding to a pseudo-isothermal elliptical mass distribution [PIEMD; (65)]. Individual cluster galaxies are selected via a multi-band selected red-sequence, and are modeled each using a dual pseudo-isothermal elliptical mass distribution [dPIE, see (66)]. The cluster galaxies are scaled according to the Faber-Jackson relation (67), but the brightest cluster galaxy (BCG), and its ellipticity, are allowed to be modified independently.

Our lens model is based on 51 multiple images of 19 background sources that are used as

constraints, 7 of which were previously known, e.g. from the CLASH survey (62, 68), and 12 are newly identified with NIRCam in the VENUS program (including the images of the SN and the host). The parameter values are optimized via a  $\chi^2$  function minimizing the distance between observed images and their predicted locations. The parameter space exploration was performed through an MCMC with stochastic moves guided by relative likelihood gradients.

The final best-fit model, minimized using 40 constraints and 21 free parameters, presents an *r.m.s.* error between the model predictions and observations of  $0.44''$ . Owing to stringent constraints requested on the position of SN Eos, the two existing images are reproduced with a precision lower than the pixel resolution ( $0.04''$ ). Due to the low input positional uncertainties, the resultant time delay and magnification uncertainties are most likely underestimated. Thus, we adopt a nominal 20% additional systematic uncertainty on both throughout. The derived magnifications and time delays, located at the model-predicted image positions, are presented in table S2.

## 6.7 Fe II pEW Measurement

To measure the pseudo-equivalent width pEW of Fe II  $\lambda 5018$ , we first smooth the spectrum using the inverse-variance Gaussian algorithm from (69). From this smoothed spectrum, we identify the local maxima in flux on either side of the absorption feature to act as the endpoints of the linear pseudo-continuum. The value of the pEW is determined within this region and the uncertainty is estimated via a simple Monte Carlo simulation, drawing simulated fluxes from the flux uncertainties at each wavelength, and varying the smoothing scale for the continuum definition. We find a Fe II  $\lambda 5018$  pEW =  $9 \pm 4 \text{ \AA}$ , a  $2.3\sigma$  detection (see Main Text Figure 2 and Figure 4). We caution that given the low resolution of the detector, blending of adjacent SN features may bias this measurement. We also caution that the phase of SN Eos where we make this measurement is very near the end of the plateau, where the ionization state is changing due to a drop in the characteristic plateau temperature of  $\sim 5000$  K (48). Nonetheless, this pEW is broadly consistent with an O3N2-derived metallicity of  $\lesssim 0.1 Z_{\odot}$  when considering that the pEW monotonically increases with phase, and is consistent with the expectation given the host luminosity.

Furthermore, we apply the same methods to measure the pEW of Fe II  $\lambda 5169$ . This feature is more strongly detected with Fe II  $\lambda 5169$  pEW =  $20 \pm 3 \text{ \AA}$ . While there may be biases associated with

deriving these values from low-resolution spectra, and we cannot rule out a potential contribution from the host galaxy [O III], we note that the Fe II absorption complex appears quite similar in morphology to the other low-metallicity local SNe-II (blue curves, Main Text Figure 4).

## 6.8 Spectroscopic Matching

We compare the two spectra of SN Eos to an extended library of low-redshift SN templates (70) using SNID-SAGE (71), a Python implementation of the original Supernova Identification [SNID, (72)] code. Both spectra matched best to the +112 and +103 day spectra of SN 1992H, a Type IIP (plateau) SN that occurred in NGC 5377. Further shared matches include the low-metallicity Type II SN 2015bs, and the Type IIP SN 2013fs.

To compare the spectra of the two images of SN Eos directly to one another, we first scale the brighter 101.2 spectrum to the 101.1 spectrum using a Markov Chain Monte Carlo (MCMC) fit assuming a Gaussian posterior and uninformed prior over the spectral range of  $2.2 - 5.5 \mu\text{m}$ . This gives a scale factor of  $0.95 \pm 0.05$ , consistent with the lens model-predicted value of  $0.85 \pm 0.26$ . Since the continuum emission is much brighter than the contribution from individual lines, this process yields consistent results when fitting to regions of the spectra that lack emission and absorption features. As shown in Main Text Figure 2, most of the commonly shared features between the spectra of the two images appear identical. We do note, however, that there appears to be a significant deviation in the flux of the  $\text{H}\alpha$  emission feature after scaling. Integrating the spectral flux density of the two spectra from  $3.97$  to  $4.13 \mu\text{m}$ , propagating the scale factor uncertainty into the significance, we find that the  $\text{H}\alpha$  flux is  $\sim 6 \sigma$  brighter for image 101.1 than image 101.2. If we instead scale the two spectra based on the observed photometry, we can derive a scale factor of  $0.874 \pm 0.005$ , in  $2 \sigma$  agreement with the value derived directly from the spectra and in strong agreement with the lens model prediction. Using this scale factor instead, the significance in the  $\text{H}\alpha$  difference is on the order of  $13 \sigma$ . We believe that this difference in  $\text{H}\alpha$  strength is most likely resulting from contamination by the host galaxy. Due to the host being resolved, the total magnification factor affecting each image is different. This difference in magnification thus results in unique amounts of host contamination in the  $\text{H}\alpha$  line for each image, resulting in inconsistent  $\text{H}\alpha$  line strengths of the combined SN + host spectra. Based on the agreement in all the other line

features, we believe that only  $\text{H}\alpha$  is significantly contaminated by the host, and we find no other evidence that could point to an alternate explanation, such as a large time delay or reduction artifact. An in-depth discussion of the underlying host contamination will be presented in Y. Asada et al. (*in prep.*).

## 6.9 SN Eos Modeling

To estimate the explosion properties of SN Eos, we compare synthetic light curves with the photometry of SN Eos presented in table S1, demagnified by a factor of  $\mu = 30\times$ . We followed the same procedures as our previous studies (73, 74) on high-redshift Type II SNe to obtain synthetic light curves. We took the red supergiant (RSG) SN progenitor models in (74) having  $0.1 \text{ Z}_\odot$ , in agreement with both the metallicity inferred from the analysis of the LAE host and directly from SN Eos itself. The RSG progenitors were computed by the stellar evolution code **Modules for Experiments in Stellar Astrophysics** (MESA) (75) and synthetic light curves were obtained by the one-dimensional multi-frequency radiation hydrodynamics code STELLA (76). In general, the shock breakout (77) luminosity in the entire early UV light curve is not expected to be as luminous as the plateau optical luminosity, as is observed in SN Eos. To power this early UV emission and match the model to observations, we embedded the explosion within a spherically symmetric, dense, and confined circumstellar medium (78) that is extended to  $10^{15} \text{ cm}$  with an enhanced mass-loss rate of  $3 \times 10^{-3} \text{ M}_\odot \text{ yr}^{-1}$ , and a wind velocity of  $10 \text{ km s}^{-1}$ .

This simplified CSM prescription does not account for the first two UV light curve points in F110W and F814W, which could be due to the shock breakout emission of a larger radii star, or interaction with an aspherical CSM (79, 80). However, due to the uncertainty in absolute magnification and lack of complimentary early-time optical data, we instead focus instead on connecting the rise in the later UV points to the optical data at  $\sim 98$  days. Our approach reasonably captures the UV light curve slopes and relative luminosities, and results in a confined CSM mass of  $0.2 \text{ M}_\odot$ . This mass is considered a lower limit, as the limited UV data prevent us from knowing whether this UV flux was near maximum during the *HST* window of observations. We obtained synthetic light curves in the observer frame by shifting synthetic spectral energy distributions to  $z = 5.133 \pm 0.001$  and convolving them with the filter response functions. Main Text Figure 5

presents an example of a resultant light-curve model for SN Eos. This iteration is an explosion of a  $16 M_{\odot}$  RSG progenitor having a hydrogen-rich envelope mass of  $10.7 M_{\odot}$  with a radius of  $593 R_{\odot}$ . It has the explosion energy of  $1.5 \times 10^{51}$  erg and the  $^{56}\text{Ni}$  mass of  $0.1 M_{\odot}$ . The  $^{56}\text{Ni}$  mass is relatively high when compared to a sample of local SNe II (81), but it is close to that estimated for SN 1987A (82). Mixing of  $^{56}\text{Ni}$  into the hydrogen-rich envelope affects the light-curve evolution (83), and we calculate two complimentary models with no mixing and full mixing, to create an envelope that matched SN Eos' observed color and late-time light curve behavior.

## 6.10 Low- $z$ Analog Comparisons

SN Eos is the farthest spectroscopically classified supernova ever discovered, and is consistent with having a very low metallicity. Thus, we compare it directly to local Universe, low-metallicity (“low- $Z$ ”) SNe II which have been suggested to be good analogs to SNe at high- $z$ , as well as to a best-matching solar metallicity SN as a control. For the low- $Z$  sample, there have only been three well-studied SNe II at  $Z \lesssim 0.1 Z_{\odot}$ : SN 2015bs (37), SN 2017ivv (38), and SN 2023ufx (39, 40). For our solar-metallicity control, we compare against SN 1992H (84), which was our best spectral template match (see Supplementary Text section 6.8). The three low- $Z$  SNe exhibit characteristics that are distinct from their solar-metallicity counterparts. Each SN was associated with a very low mass host galaxy, consistent with their low metallicity, having optical peaks  $\sim 0.7 - 1.7$  brighter than the average [ $\bar{M}_B = -16.80 \pm 0.37$  AB mag; (41)], as well as faster declining plateau phases ( $\sim 40 - 50$  vs  $\sim 100$  days) than the bulk of the population reported in the literature [see the following non-exhaustive list, (23, 48, 85, 86)]. In the case of SN Eos, we find that our model light curve has properties that span this comparison sample, with our inferred peak magnitude being similarly brighter than average ( $-17.7$  AB mag), however, with a long duration plateau more closely matching SN 1992H [as well as other typical, local SNe II (48)].

Main Text Figure 2 compares SN Eos to these four SNe, selected at a similar phases ( $\gtrsim 98$  days) to our spectral observation of SN Eos. The exception is SN 2015bs, which we plot at a phase of +57 days from explosion, because the spectrum at +76 days did not have high enough signal-to-noise to compare Fe II. Remarkably, we find that SN Eos overall compares most favorably to SN 1992H, especially in terms of its H $\alpha$  and Na I doublet (rest-frame  $\approx 5892 \text{ \AA}$ ) features. The

disparity in H $\alpha$  between SN Eos and SN 2017ivv may be due to a difference in phase, however, the boxy shape of SN 2023ufx's H $\alpha$  profile may indicate further interaction with an extended medium at  $\sim 98$  days[ (87), although see the discussion in (39)]. Such features are not apparent in the spectrum of SN Eos. In the right-hand panel of Main Text Figure 2 , we focus on the Fe II absorption feature of each SN, and find extremely good agreement with all three low-Z SNe in the pEW of Fe II (including with SN 2015bs despite only comparing the +57 day spectrum), whereas the absorption for SN 1992H is much deeper. More detailed comparisons between these SNe and SN Eos will require additional data: photometric observations of SN Eos' decline off of the plateau, as well as nebular spectra, will constrain the amount of  $^{56}\text{Ni}$  synthesized, and therefore the core mass of the progenitor. Combining this with the envelope mass estimate from the plateau duration will enable a more confident inference on the zero-age main sequence mass of the progenitor to SN Eos, potentially holding implications for the IMF at  $z > 5$ .

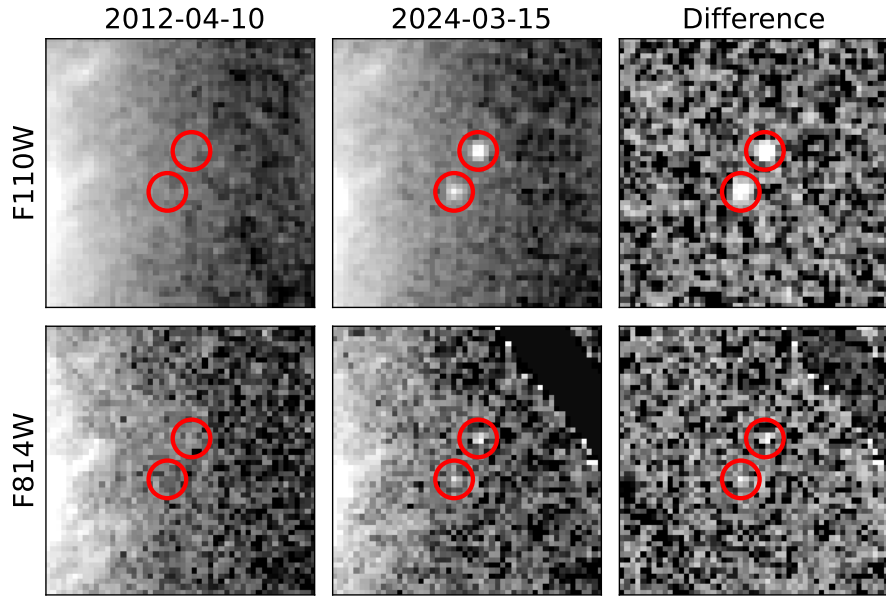


**Figure S1: The archival detection of SN Eos in *HST* imaging, described in Supplementary Text section 6.2.** The top row shows the F110W filter, and the bottom row shows the F814W filter. Template imaging from 2012 (left column) shows no point source, while subsequent imaging from 2024 has clear detections of both SN images. The right column shows the difference between the 2024 and 2012 observations.

PID	MJD	Instrument	Filter/Grating	101.1 (AB mag)	101.2 (AB mag)
17504	60380.1	<i>HST</i> /WFC3-UVIS	<i>F814W</i>	$26.40 \pm 0.16$	$26.08 \pm 0.12$
17504	60380.1	<i>HST</i> /WFC3-IR	<i>F110W</i>	$25.51 \pm 0.05$	$24.81 \pm 0.04$
17504	60382.1	<i>HST</i> /WFC3-UVIS	<i>F814W</i>	$26.61 \pm 0.34$	$26.30 \pm 0.27$
17504	60382.1	<i>HST</i> /WFC3-IR	<i>F110W</i>	$25.37 \pm 0.06$	$24.83 \pm 0.04$
17504	60384.1	<i>HST</i> /WFC3-UVIS	<i>F814W</i>	$26.23 \pm 0.25$	$25.91 \pm 0.20$
17504	60384.1	<i>HST</i> /WFC3-IR	<i>F110W</i>	$25.59 \pm 0.12$	$25.04 \pm 0.07$
17504	60386.2	<i>HST</i> /WFC3-UVIS	<i>F814W</i>	$25.63 \pm 0.27$	$26.04 \pm 0.35$
17504	60386.2	<i>HST</i> /WFC3-IR	<i>F110W</i>	$25.45 \pm 0.15$	$24.74 \pm 0.09$
17504	60387.0	<i>HST</i> /WFC3-IR	<i>F110W</i>	$25.51 \pm 0.18$	$24.57 \pm 0.08$
6882	60919.0	<i>JWST</i> /NIRCam	<i>F090W</i>	$> 28.0$	$> 28.0$
6882	60919.0	<i>JWST</i> /NIRCam	<i>F115W</i>	$> 28.0$	$> 28.0$
6882	60919.0	<i>JWST</i> /NIRCam	<i>F150W</i>	$> 28.0$	$> 28.0$
6882	60919.0	<i>JWST</i> /NIRCam	<i>F200W</i>	$> 28.0$	$> 28.0$
6882	60919.0	<i>JWST</i> /NIRCam	<i>F210M</i>	$> 28.0$	$> 28.0$
6882	60919.1	<i>JWST</i> /NIRCam	<i>F277W</i>	$26.80 \pm 0.01$	$26.63 \pm 0.03$
6882	60919.1	<i>JWST</i> /NIRCam	<i>F300M</i>	$26.27 \pm 0.01$	$26.25 \pm 0.03$
6882	60919.1	<i>JWST</i> /NIRCam	<i>F356W</i>	$25.94 \pm 0.01$	$25.81 \pm 0.02$
6882	60919.0	<i>JWST</i> /NIRCam	<i>F410M</i>	$25.27 \pm 0.01$	$25.26 \pm 0.01$
6882	60919.1	<i>JWST</i> /NIRCam	<i>F444W</i>	$25.44 \pm 0.01$	$25.25 \pm 0.01$
9493	60956.6	<i>JWST</i> /NIRCam	<i>F070W</i>	$> 27.5$	$> 27.5$
9493	60956.6	<i>JWST</i> /NIRCam	<i>F277W</i>	$27.21 \pm 0.01$	$27.11 \pm 0.05$
9493	60956.6	<i>JWST</i> /NIRCam	<i>F356W</i>	$26.20 \pm 0.01$	$26.07 \pm 0.03$
9493	60956.6	<i>JWST</i> /NIRCam	<i>F444W</i>	$25.63 \pm 0.01$	$25.51 \pm 0.02$
9493	60956.6	<i>JWST</i> /NIRSpec	<i>PRISM</i>	–	–

**Table S1: All observations of SN Eos.** Columns are: (i) *HST/JWST* Program ID, (ii) Modified Julian date, (iii) *JWST/HST* instrument, (iv) WFC3/NIRCam filter, (v) & (vi) photometry from lens image 101.1 and 101.2 for SN Eos in AB mag. Upper limits are  $5\sigma$ .

Image	$\alpha$	$\delta$	$ \mu $	$\tau$
	[deg, J2000]	[deg, J2000]		[time, observer]
101.1	292.9550834	-26.5748399	$25.46 \pm 5.73$	0
101.2	292.9549276	-26.5746208	$29.88 \pm 6.22$	$0.99 \pm 0.33$ days
p101.3	292.9516835	-26.5782154	$12.93 \pm 2.59$	$-3.68 \pm 0.74$ years
p101.4	292.9532987	-26.5793043	$13.01 \pm 2.91$	$-3.49 \pm 0.70$ years
p101.5	292.9683686	-26.5760254	$2.15 \pm 0.43$	$-53.99 \pm 10.80$ years

**Table S2: Summary of the detected and predicted images of SN Eos.** Predicted images are preceded with a ‘p’. Columns are: (i) Object Id; (ii) & (iii) R.A. and Dec. in degrees; (iv) Lensing magnification  $\mu$  for the MCMC-resultant average; (v) Relative time delay  $\tau$  in the observer frame, measured from the arrival of image 101.1, for the MCMC-resultant average. Image 101.2 is estimated to be the last one to arrive.

## References and Notes

1. S. E. I. Bosman, *et al.*, Hydrogen reionization ends by  $z = 5.3$ : Lyman- $\alpha$  optical depth measured by the XQR-30 sample. *MNRAS* **514** (1), 55–76 (2022), doi:10.1093/mnras/stac1046.
2. R. H. Becker, *et al.*, Evidence for Reionization at  $z \sim 6$ : Detection of a Gunn-Peterson Trough in a  $z=6.28$  Quasar. *AJ* **122** (6), 2850–2857 (2001), doi:10.1086/324231.
3. P. Dayal, A. Ferrara, Early galaxy formation and its large-scale effects. *Phys. Rep.* **780**, 1–64 (2018), doi:10.1016/j.physrep.2018.10.002.
4. D. Ceverino, A. Klypin, The Role of Stellar Feedback in the Formation of Galaxies. *ApJ* **695** (1), 292–309 (2009), doi:10.1088/0004-637X/695/1/292.
5. R. A. Windhorst, *et al.*, On the Observability of Individual Population III Stars and Their Stellar-mass Black Hole Accretion Disks through Cluster Caustic Transits. *ApJS* **234** (2), 41

(2018), doi:10.3847/1538-4365/aaa760.

6. K. Nakajima, *et al.*, JWST Census for the Mass-Metallicity Star Formation Relations at  $z = 4\text{--}10$  with Self-consistent Flux Calibration and Proper Metallicity Calibrators. *ApJS* **269** (2), 33 (2023), doi:10.3847/1538-4365/acd556.
7. T. Karlsson, V. Bromm, J. Bland-Hawthorn, Pregalactic metal enrichment: The chemical signatures of the first stars. *Reviews of Modern Physics* **85** (2), 809–848 (2013), doi:10.1103/RevModPhys.85.809.
8. L. Dessart, *et al.*, Type II Plateau supernovae as metallicity probes of the Universe. *MNRAS* **440** (2), 1856–1864 (2014), doi:10.1093/mnras/stu417.
9. S. Fujimoto, *et al.*, Vast Exploration for Nascent, Unexplored Sources (VENUS), JWST Proposal. Cycle 4, ID. #6882 (2025).
10. P. Natarajan, *et al.*, Strong Lensing by Galaxy Clusters. *Space Sci. Rev.* **220** (2), 19 (2024), doi:10.1007/s11214-024-01051-8.
11. S. Refsdal, On the Possibility of Determining Hubble’s Parameter and the Masses of Galaxies from the Gravitational Lens Effect. *Monthly Notices of the Royal Astronomical Society* **128** (4), 307–310 (1964), doi:10.1093/mnras/128.4.307, <https://academic.oup.com/mnras/article/128/4/307/2601707>.
12. T. Treu, P. J. Marshall, Time delay cosmography. *The Astronomy and Astrophysics Review* **24** (1), 11 (2016), doi:10.1007/s00159-016-0096-8, <http://link.springer.com/10.1007/s00159-016-0096-8>.
13. J. M. Diego, *et al.*, Dark Matter under the Microscope: Constraining Compact Dark Matter with Caustic Crossing Events. *ApJ* **857** (1), 25 (2018), doi:10.3847/1538-4357/aab617.
14. L. L. R. Williams, *et al.*, Flashlights: Properties of Highly Magnified Images Near Cluster Critical Curves in the Presence of Dark Matter Subhalos. *ApJ* **961** (2), 200 (2024), doi:10.3847/1538-4357/ad1660.

15. B. Welch, *et al.*, A highly magnified star at redshift 6.2. *Nature* **603** (7903), 815–818 (2022), doi:10.1038/s41586-022-04449-y.
16. J. M. Diego, *et al.*, Godzilla, a monster lurks in the Sunburst galaxy. *A&A* **665**, A134 (2022), doi:10.1051/0004-6361/202243605.
17. W. Chen, *et al.*, Shock cooling of a red-supergiant supernova at redshift 3 in lensed images. *\nat* **611** (7935), 256–259 (2022), doi:10.1038/s41586-022-05252-5.
18. B. I. Ciocan, *et al.*, The VLT-MUSE and ALMA view of the MACS 1931.8-2635 brightest cluster galaxy. *A&A* **649**, A23 (2021), doi:10.1051/0004-6361/202040010.
19. Materials and methods are available as supplementary material.
20. P. J. Brown, *et al.*, Ultraviolet Light Curves of Supernovae with the Swift Ultraviolet/Optical Telescope. *AJ* **137** (5), 4517–4525 (2009), doi:10.1088/0004-6256/137/5/4517.
21. T. A. Pritchard, P. W. A. Roming, P. J. Brown, A. J. Bayless, L. H. Frey, Bolometric and UV Light Curves of Core-collapse Supernovae. *ApJ* **787** (2), 157 (2014), doi:10.1088/0004-637X/787/2/157.
22. K. A. Bostroem, *et al.*, SN 2022acko: The First Early Far-ultraviolet Spectra of a Type IIP Supernova. *ApJ* **953** (2), L18 (2023), doi:10.3847/2041-8213/ace31c.
23. J. P. Anderson, *et al.*, Characterizing the V-band Light-curves of Hydrogen-rich Type II Supernovae. *ApJ* **786** (1), 67 (2014), doi:10.1088/0004-637X/786/1/67.
24. D. J. Schlegel, D. P. Finkbeiner, M. Davis, Maps of Dust Infrared Emission for Use in Estimation of Reddening and Cosmic Microwave Background Radiation Foregrounds. *ApJ* **500** (2), 525–553 (1998), doi:10.1086/305772.
25. E. F. Schlafly, D. P. Finkbeiner, Measuring Reddening with Sloan Digital Sky Survey Stellar Spectra and Recalibrating SFD. *ApJ* **737** (2), 103 (2011), doi:10.1088/0004-637X/737/2/103.
26. D. W. Hogg, I. K. Baldry, M. R. Blanton, D. J. Eisenstein, The K correction. *arXiv e-prints* astro-ph/0210394 (2002), doi:10.48550/arXiv.astro-ph/0210394.

27. A. Saxena, *et al.*, JADES: The production and escape of ionizing photons from faint Lyman-alpha emitters in the epoch of reionization. *A&A* **684**, A84 (2024), doi:10.1051/0004-6361/202347132.
28. D. Ďurovčíková, *et al.*, An Extremely Metal-poor Ly $\alpha$  Emitter Candidate at  $z = 6$  Revealed through Absorption Spectroscopy. *ApJ* **987** (2), L33 (2025), doi:10.3847/2041-8213/ade71c.
29. T. Morishita, *et al.*, Pristine Massive Star Formation Caught at the Break of Cosmic Dawn. *arXiv e-prints* arXiv:2507.10521 (2025), doi:10.48550/arXiv.2507.10521.
30. E. Vanzella, *et al.*, A Pristine Star-Forming Complex at  $z=4.19$ . *arXiv e-prints* arXiv:2509.07073 (2025), doi:10.48550/arXiv.2509.07073.
31. C. J. Willott, *et al.*, In Search of the First Stars: An Ultra-compact and Very-low-metallicity Ly $\alpha$  Emitter Deep within the Epoch of Reionization. *ApJ* **988** (1), 26 (2025), doi:10.3847/1538-4357/addf49.
32. L. Dessart, D. J. Hillier, Non-LTE time-dependent spectroscopic modelling of Type II-plateau supernovae from the photospheric to the nebular phase: case study for 15 and 25  $M_\odot$  progenitor stars. *MNRAS* **410** (3), 1739–1760 (2011), doi:10.1111/j.1365-2966.2010.17557.x.
33. L. Dessart, D. J. Hillier, R. Waldman, E. Livne, Type II-Plateau supernova radiation: dependences on progenitor and explosion properties. *MNRAS* **433** (2), 1745–1763 (2013), doi:10.1093/mnras/stt861.
34. J. P. Anderson, *et al.*, Type II supernovae as probes of environment metallicity: observations of host H II regions. *A&A* **589**, A110 (2016), doi:10.1051/0004-6361/201527691.
35. F. Taddia, *et al.*, Metallicity from Type II supernovae from the (I)PTF. *A&A* **587**, L7 (2016), doi:10.1051/0004-6361/201527983.
36. C. P. Gutiérrez, *et al.*, Type II supernovae in low-luminosity host galaxies. *MNRAS* **479** (3), 3232–3253 (2018), doi:10.1093/mnras/sty1581.
37. J. P. Anderson, *et al.*, The lowest-metallicity type II supernova from the highest-mass red supergiant progenitor. *Nature Astronomy* **2**, 574–579 (2018), doi:10.1038/s41550-018-0458-4.

38. C. P. Gutiérrez, *et al.*, SN 2017ivv: two years of evolution of a transitional Type II supernova. *MNRAS* **499** (1), 974–992 (2020), doi:10.1093/mnras/staa2763.

39. M. A. Tucker, *et al.*, The Extremely Metal-poor SN 2023ufx: A Local Analog to High-redshift Type II Supernovae. *ApJ* **976** (2), 178 (2024), doi:10.3847/1538-4357/ad8448.

40. A. P. Ravi, *et al.*, Luminous Type II Short-plateau SN 2023ufx: Asymmetric Explosion of a Partially Stripped Massive Progenitor. *ApJ* **982** (1), 12 (2025), doi:10.3847/1538-4357/adb0bb.

41. D. Richardson, R. L. Jenkins, III, J. Wright, L. Maddox, Absolute-magnitude Distributions of Supernovae. *AJ* **147** (5), 118 (2014), doi:10.1088/0004-6256/147/5/118.

42. J. P. Anderson, *et al.*, Analysis of blueshifted emission peaks in Type II supernovae. *MNRAS* **441** (1), 671–680 (2014), doi:10.1093/mnras/stu610.

43. C. P. Gutiérrez, *et al.*, H <sub>$\alpha$</sub>  Spectral Diversity of Type II Supernovae: Correlations with Photometric Properties. *ApJ* **786** (2), L15 (2014), doi:10.1088/2041-8205/786/2/L15.

44. A. Heger, C. L. Fryer, S. E. Woosley, N. Langer, D. H. Hartmann, How Massive Single Stars End Their Life. *ApJ* **591** (1), 288–300 (2003), doi:10.1086/375341.

45. D. Sanyal, N. Langer, D. Szécsi, S. -C Yoon, L. Grassitelli, Metallicity dependence of envelope inflation in massive stars. *A&A* **597**, A71 (2017), doi:10.1051/0004-6361/201629612.

46. C. P. Gutiérrez, *et al.*, Type II Supernova Spectral Diversity. I. Observations, Sample Characterization, and Spectral Line Evolution. *ApJ* **850** (1), 89 (2017), doi:10.3847/1538-4357/aa8f52.

47. F. Taddia, *et al.*, The Carnegie Supernova Project I. Analysis of stripped-envelope supernova light curves. *\aap* **609**, A136 (2018), doi:10.1051/0004-6361/201730844.

48. L. Martinez, *et al.*, Type II supernovae from the Carnegie Supernova Project-I. I. Bolometric light curves of 74 SNe II using uBgVriYJH photometry. *A&A* **660**, A40 (2022), doi:10.1051/0004-6361/202142075.

49. C. A. Tremonti, *et al.*, The Origin of the Mass-Metallicity Relation: Insights from 53,000 Star-forming Galaxies in the Sloan Digital Sky Survey. *ApJ* **613** (2), 898–913 (2004), doi:10.1086/423264.

50. J. Kim, *et al.*, Low-surface-brightness Galaxies are Missing in the Observed Stellar Mass Function. *ApJ* **951** (2), 137 (2023), doi:10.3847/1538-4357/acd251.

51. G. Brammer, grizli (2023), doi:10.5281/zenodo.1146904.

52. L. D. Bradley, *et al.*, High-redshift Galaxy Candidates at  $z = 9\text{--}10$  as Revealed by JWST Observations of WHL0137-08. *ApJ* **955** (1), 13 (2023), doi:10.3847/1538-4357/acecf6.

53. J. Rigby, *et al.*, The Science Performance of JWST as Characterized in Commissioning. *PASP* **135** (1046), 048001 (2023), doi:10.1088/1538-3873/acb293.

54. R. Endsley, *et al.*, A JWST/NIRCam study of key contributors to reionization: the star-forming and ionizing properties of UV-faint  $z = 7\text{--}8$  galaxies. *MNRAS* **524** (2), 2312–2330 (2023), doi:10.1093/mnras/stad1919.

55. V. Kokorev, *et al.*, A Glimpse of the New Redshift Frontier through AS1063. *ApJ* **983** (1), L22 (2025), doi:10.3847/2041-8213/adc458.

56. P. Kelly, *et al.*, SNAP Survey for Strongly Lensed Supernovae and Magnified Stars, HST Proposal. Cycle 31, ID. #17504 (2023).

57. G. Brammer, msaexp: NIRSpec analysis tools (2023), doi:10.5281/zenodo.8319596.

58. K. Michalewicz, M. Millon, F. Dux, F. Courbin, STARRED: a two-channel deconvolution method with Starlet regularization. *The Journal of Open Source Software* **8** (85), 5340 (2023), doi:10.21105/joss.05340.

59. M. Millon, K. Michalewicz, F. Dux, F. Courbin, P. J. Marshall, Image Deconvolution and Point-spread Function Reconstruction with STARRED: A Wavelet-based Two-channel Method Optimized for Light-curve Extraction. *AJ* **168** (2), 55 (2024), doi:10.3847/1538-3881/ad4da7.

60. J.-L. Starck, F. Murtagh, M. Bertero, Starlet Transform in Astronomical Data Processing, in *Handbook of Mathematical Methods in Imaging*, O. Scherzer, Ed. (Springer), pp. 2053–2098 (2015), doi:10.1007/978-1-4939-0790-8\_59.

61. J. D. R. Pierel, *et al.*, Cosmology with supernova Encore in the strong lensing cluster MACS J0138-2155: Time delays & Hubble constant measurement. *arXiv e-prints* p. arXiv:2509.12301 (2025), [eprint](#): 2509.12301, doi:10.48550/arXiv.2509.12301.

62. A. Zitrin, *et al.*, Hubble Space Telescope Combined Strong and Weak Lensing Analysis of the CLASH Sample: Mass and Magnification Models and Systematic Uncertainties. *ApJ* **801**, 44 (2015), doi:10.1088/0004-637X/801/1/44.

63. M. Pascale, *et al.*, Unscrambling the lensed galaxies in JWST images behind SMACS0723. *arXiv e-prints* arXiv:2207.07102 (2022).

64. L. J. Furtak, *et al.*, UNCOVERing the extended strong lensing structures of Abell 2744 with the deepest JWST imaging. *arXiv e-prints* arXiv:2212.04381 (2022).

65. C. R. Keeton, Computational Methods for Gravitational Lensing. *ArXiv Astrophysics e-prints* (2001).

66. Á. Elíasdóttir, *et al.*, Where is the matter in the Merging Cluster Abell 2218? *arXiv e-prints* arXiv:0710.5636 (2007).

67. S. M. Faber, R. E. Jackson, Velocity dispersions and mass-to-light ratios for elliptical galaxies. *ApJ* **204**, 668–683 (1976), doi:10.1086/154215.

68. M. Postman, *et al.*, The Cluster Lensing and Supernova Survey with Hubble: An Overview. *ApJS* **199** (2), 25 (2012), doi:10.1088/0067-0049/199/2/25.

69. D. Branch, *et al.*, Comparative Direct Analysis of Type Ia Supernova Spectra. II. Maximum Light. *PASP* **118** (842), 560–571 (2006), doi:10.1086/502778.

70. D. Magill, *et al.*, Super-SNID: An Expanded Set of SNID Classes and Templates for the New Era of Wide-field Surveys. *Research Notes of the American Astronomical Society* **9** (4), 78 (2025), doi:10.3847/2515-5172/adcab6.

71. F. Stoppa, SNID SAGE: A Modern Framework for Interactive Supernova Classification and Spectral Analysis (In Prep, 2025), <https://github.com/FiorenSt/SNID-SAGE>.

72. S. Blondin, J. L. Tonry, Determining the Type, Redshift, and Age of a Supernova Spectrum. *ApJ* **666** (2), 1024–1047 (2007), doi:10.1086/520494.

73. D. A. Coulter, *et al.*, Discovery of a likely Type II SN at  $z=3.6$  with JWST. *arXiv e-prints* p. arXiv:2501.05513 (2025), eprint: 2501.05513, doi:10.48550/arXiv.2501.05513.

74. T. J. Moriya, *et al.*, Properties of high-redshift Type II supernovae discovered by the JADES transient survey. *PASJ* **77** (4), 851–862 (2025), doi:10.1093/pasj/psaf052.

75. B. Paxton, *et al.*, Modules for Experiments in Stellar Astrophysics (MESA). *ApJS* **192** (1), 3 (2011), doi:10.1088/0067-0049/192/1/3.

76. S. Blinnikov, P. Lundqvist, O. Bartunov, K. Nomoto, K. Iwamoto, Radiation Hydrodynamics of SN 1987A. I. Global Analysis of the Light Curve for the First 4 Months. *ApJ* **532** (2), 1132–1149 (2000), doi:10.1086/308588.

77. T. J. Moriya, B. M. Subrayan, D. Milisavljevic, S. I. Blinnikov, Synthetic red supergiant explosion model grid for systematic characterization of Type II supernovae. *PASJ* **75** (3), 634–645 (2023), doi:10.1093/pasj/psad024.

78. F. Förster, *et al.*, The delay of shock breakout due to circumstellar material evident in most type II supernovae. *Nature Astronomy* **2**, 808 (2018), doi:10.1038/s41550-018-0563-4.

79. A. Singh, *et al.*, Unravelling the Asphericities in the Explosion and Multifaceted Circumstellar Matter of SN 2023ixf. *ApJ* **975** (1), 132 (2024), doi:10.3847/1538-4357/ad7955.

80. Y. Yang, *et al.*, An axisymmetric shock breakout indicated by prompt polarized emission from the type II supernova 2024ggi. *arXiv e-prints* arXiv:2511.08824 (2025), doi:10.48550/arXiv.2511.08824.

81. J. P. Anderson, A meta-analysis of core-collapse supernova  $^{56}\text{Ni}$  masses. *A&A* **628**, A7 (2019), doi:10.1051/0004-6361/201935027.

82. I. R. Seitenzahl, F. X. Timmes, G. Magkotsios, The Light Curve of SN 1987A Revisited: Constraining Production Masses of Radioactive Nuclides. *ApJ* **792** (1), 10 (2014), doi:10.1088/0004-637X/792/1/10.

83. A. Kozyreva, E. Nakar, R. Waldman, The role of radioactive nickel in shaping the plateau phase of Type II supernovae. *MNRAS* **483** (1), 1211–1223 (2019), doi:10.1093/mnras/sty3185.
84. A. Clocchiatti, *et al.*, A Study of SN 1992H in NGC 5377. *AJ* **111**, 1286 (1996), doi:10.1086/117874.
85. L. Martinez, *et al.*, Type II supernovae from the Carnegie Supernova Project-I. II. Physical parameter distributions from hydrodynamical modelling. *A&A* **660**, A41 (2022), doi:10.1051/0004-6361/202142076.
86. L. Martinez, *et al.*, Type II supernovae from the Carnegie Supernova Project-I. III. Understanding SN II diversity through correlations between physical and observed properties. *A&A* **660**, A42 (2022), doi:10.1051/0004-6361/202142555.
87. L. Dessart, D. J. Hillier, Modeling the signatures of interaction in Type II supernovae: UV emission, high-velocity features, broad-boxy profiles. *A&A* **660**, L9 (2022), doi:10.1051/0004-6361/202243372.